Journal of Colloid and Interface Science 649 (2023) 844–854

Contents lists available at ScienceDirect

Journal of Colloid And Interface Science

journal homepage: www.elsevier.com/locate/jcis

Low-dose albumin-coated gold nanorods induce intercellular gaps on vascular endothelium by causing the contraction of cytoskeletal actin

Zhengqiang Li [a,b,1], Jinyuan Liu [a,b,1], Katherine Ballard [a,b], Chao Liang [c,d,*], Congzhou Wang [a,b,*]

[a] Nanoscience and Biomedical Engineering, South Dakota School of Mines and Technology, 501 E St Joseph Street, Rapid City, SD 57701, USA
[b] BioSystems Networks & Translational Research (BioSNTR), 501 E St Joseph Street, Rapid City, SD 57701, USA
[c] Department of Anesthesiology, Zhongshan Hospital (Xiamen) Fudan University, Xiamen 361015, China
[d] Department of Anesthesiology, Zhongshan Hospital, Fudan University, Shanghai 200032, China

GRAPHICAL ABSTRACT

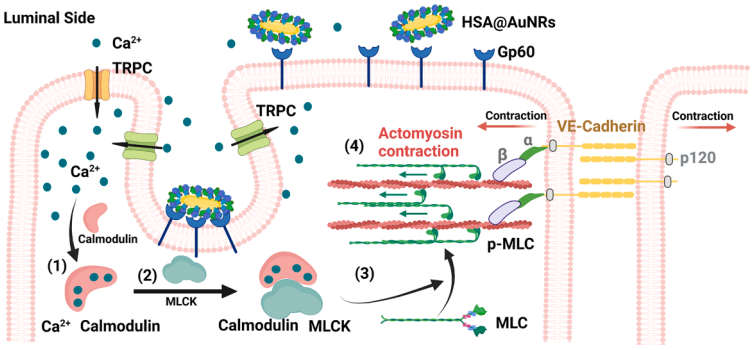

ARTICLE INFO

Keywords:
Albumin-coated gold nanorods
Vascular endothelial cells
Intercellular gaps
Calcium influx
Actomyosin contraction

ABSTRACT

Cytotoxicity of nanoparticles, typically evaluated by biochemical-based assays, often overlook the cellular biophysical properties such as cell morphology and cytoskeletal actin, which could serve as more sensitive indicators for cytotoxicity. Here, we demonstrate that low-dose albumin-coated gold nanorods (HSA@AuNRs), although being considered noncytotoxic in multiple biochemical assays, can induce intercellular gaps and enhance the paracellular permeability between human aortic endothelial cells (HAECs). The formation of intercellular gaps can be attributed to the changed cell morphology and cytoskeletal actin structures, as validated at the monolayer and single cell levels using fluorescence staining, atomic force microscopy, and super-resolution imaging. Molecular mechanistic study shows the caveolae-mediated endocytosis of HSA@AuNRs induces the calcium influx and activates actomyosin contraction in HAECs. Considering the important roles of endothelial integrity/dysfunction in various physiological/pathological conditions, this work suggests a potential adverse effect of albumin-coated gold nanorods on the cardiovascular system. On the other hand, this work also offers a feasible way to modulate the endothelial permeability, thus promoting drug and nanoparticle delivery across the endothelium.

* Corresponding authors at: Department of Anesthesiology, Zhongshan Hospital (Xiamen) Fudan University, Xiamen 361015, China (C. Liang). Nanoscience and Biomedical Engineering, South Dakota School of Mines and Technology, 501 E St Joseph Street, Rapid City, SD 57701, USA (C. Wang).
E-mail addresses: superwm226@126.com (C. Liang), congzhou.wang@sdsmt.edu (C. Wang).
[1] Z. L. and J. L. contributed equally to this work.

https://doi.org/10.1016/j.jcis.2023.06.154
Received 17 March 2023; Received in revised form 17 June 2023; Accepted 22 June 2023
Available online 24 June 2023

1. Introduction

Nanoparticles interact with human cells, owing to unintended leakage of nanoparticles into the environment (e.g., water and air pollution), or intended diagnostic and therapeutic applications (e.g., tumor targeting). Exposing cells to nanoparticles can cause dose-dependent cytotoxic effects. Conventionally, such effects are characterized using biochemical-based cytotoxicity assays, including cell viability assays that measure the metabolic activity of mitochondria and membrane integrity assays which quantify the leaked cytoplasmic enzyme owing to the disruption of plasma membrane [1–4]. As the old adage goes, "the dose makes the poison", nanoparticle dose that does not cause significant damage to plasma membrane and viability of cells is typically defined to be a safe, noncytotoxic dose [5]. However, a growing number of studies indicated that the conventional biochemical-based assays might underestimate the cytotoxicity of nanoparticles due to the limited assay sensitivity [6–7]. For instance, a pioneering work showed that anionic polymer-coated gold nanospheres can cause abnormality in cell morphology and cytoskeletal structure at the lower-doses than the inception of decreased cell viability and membrane integrity, suggesting that cell morphology and cytoskeletal structure could serve as more sensitive indicators to characterize the cytotoxicity of nanoparticles [6,8]. From the toxicological perspective, this is particularly noteworthy as the change of cell morphology and cytoskeleton could lead to many pathological conditions [9–11]. Therefore, it is critical to pay more attention to the effect of low-dose nanoparticles on cell morphology and cytoskeleton - the cytotoxic effects that are often overlooked by the conventional biochemical-based assays.

Gold nanoparticles, especially gold nanorods (AuNRs), received increased enthusiasm in the medical field thanks to excellent biocompatibility, tunable size, shape, surface chemistry, and photothermal effect [12–18]. Currently, there are multiple on-going clinical trials using intravenously injected gold nanorods to passively target solid tumors for conducting photothermal therapy [19]. To ensure the good biocompatibility and colloidal stability of gold nanoparticles, the common practice is to replace the more cytotoxic capping agent (i.e., surface surfactant) from the synthesis of gold nanoparticles with less cytotoxic polymers [20–21]. The most representative example is to coat gold nanoparticles with polyethylene glycol (PEG), which not only removes the initial cytotoxic surfactant from the nanoparticle surface, but also avoids forming protein corona and prolongs circulation life of the nanoparticles [22–23]. Here, the non-fouling property of the PEG coating is tightly related to a hydrating layer around the surface, which forms energetic and physical barriers to minimize protein adsorption onto the surface [24]. Unfortunately, recent studies revealed that the administration of PEGylated nanoparticles/drugs results in the generation of anti-PEG antibodies and immune response, making this approach questionable for *in vivo* applications [25–26]. As an alternative solution, coating nanoparticles with albumin protein has attracted much interest lately because of its non-immunogenicity (as the most abundant serum protein) and ability to resist protein adsorption using a similar non-fouling mechanism as PEG does [27–29]. Another important advantage of albumin coating lies in its preferential tumor accumulation because of the strong binding between albumin and a tumor secreted protein, named SPARC [30]. With these considerations, albumin-coated gold nanoparticles have been considered as a promising platform for cancer treatment, while the potential adverse effect of albumin-coated gold nanoparticles, especially at low doses, are rarely studied and reported.

In this work, we focus on the effect of low-dose albumin-coated gold nanorods on the vascular endothelial cells. The rationale of choosing these cells as the cell model is that most *in vivo* applications of gold nanorods are based on the intravenous injection, which leads to the direct interaction between nanorods and endothelial cells that lines the interior wall of vascular structures [31]. We particularly selected human aortic endothelial cells (HAECs) owing to their suitability in the studies of endothelial dysfunction and cardiovascular diseases caused by air pollution, oxidative stress, inflammation, and nanomaterial exposure [32–35]. We first identified several noncytotoxic doses of albumin-coated gold nanorods using a series of biochemical assays. Interestingly, these low doses of albumin-coated gold nanorods, although deemed to be noncytotoxic/safe in these assays, were still found to cause the intercellular gaps between endothelial cells. Further single cell imaging and molecular mechanism studies demonstrated that the low doses of albumin-coated gold nanorods enhanced the endothelial permeability by causing the contraction of cytoskeletal actin. Considering the critical roles of endothelial integrity/dysfunction in various physiological/pathological conditions [36–37], our work suggests a potential adverse effect of low-dose albumin-coated gold nanorods. From the nanotoxicological perspective, the cellular morphological and cytoskeletal features may offer more sensitive, alternative measures to determine the safety and cytotoxicity of nanoparticles in vitro.

2. Results and discussion

2.1. Preparation and characterization of albumin-coated gold nanorods

Gold nanorods (AuNRs) were synthesized using a seed-mediated method having hexadecyltrimethylammonium bromide (CTAB) as the capping agent [38–40]. To coat the surface of AuNRs with human serum albumin (HSA), we performed a ligand exchange approach established in our group to gradually replace the CTAB molecules with HSA as illustrated in Fig. 1**A** [41]. This approach allows the complete removal of cytotoxic CTAB and uniform coverage of protein molecules on the nanorod surface [42–43]. As shown in Fig. 1**B**, transmission electron microscopy (TEM) images displayed a uniform coating with ~ 3 nm thickness surrounding the nanorods, suggesting a monolayer of HSA was coated on the nanorod surface. Statistical analysis of individual nanorods in TEM images showed the size of CTAB-capped gold nanorods (CTAB@AuNRs) slightly increased following the surface coating of HSA (HSA@AuNRs). Specifically, the length of AuNRs increased from 47.3 ± 4.9 to 52.5 ± 3.6 nm, and the diameter of AuNRs rose from 12.5 ± 1.2 to 18.3 ± 1.6 nm (Fig. 1**C**). Bicinchoninic acid assay showed there are ~80 HSA molecules adsorbed on each nanorod surface (**Supporting information**).

The successful preparation of HSA@AuNRs was further validated by the UV–vis spectroscopy, dynamic light scattering (DLS), and Zeta potential measurements (Fig. 1**D-1F**). After coating with HSA monolayer, the extinction peak of AuNRs exhibited a redshift (774 → 787 nm) due to the increase of refractive index surrounding the nanorod surface (Fig. 1**D**) [44]. The 787 nm peak wavelength here falls into the near-infrared window, which makes the HSA@AuNRs suitable for photothermal therapy. DLS spectra also showed the hydrodynamic size of AuNRs in water (pH = 7) increased from 58 to 68 nm (Fig. 1**E**), and Zeta potential switched from +46 to −24.6 mV owing to surface ligand exchange from positive-charged CTAB to negative-charged HSA molecules (Fig. 1**F**). Apart from surface coating characterization, DLS and Zeta potential measurements also revealed excellent colloidal stability of HSA@AuNRs in cell culture medium (pH = 7.2), demonstrated by the slightly increased hydrodynamic size and Zeta potential, probably owing to the adsorption of protein molecules from cell culture medium to the nanorod surface. The hydrodynamic size of HSA@AuNRs in cell culture medium did not show obvious change within 7 days, further confirming the superior colloidal stability of as-prepared HSA@AuNRs (**Fig. S1**). Together, these results suggest the successful preparation of albumin-coated gold nanorods (HSA@AuNRs) with excellent colloidal stability in physiological fluids.

2.2. Cytotoxicity and cell uptake of albumin-coated gold nanorods

The cytotoxicity of albumin-coated gold nanorods on human aortic endothelial cells (HAECs) was assessed using a panel of routinely

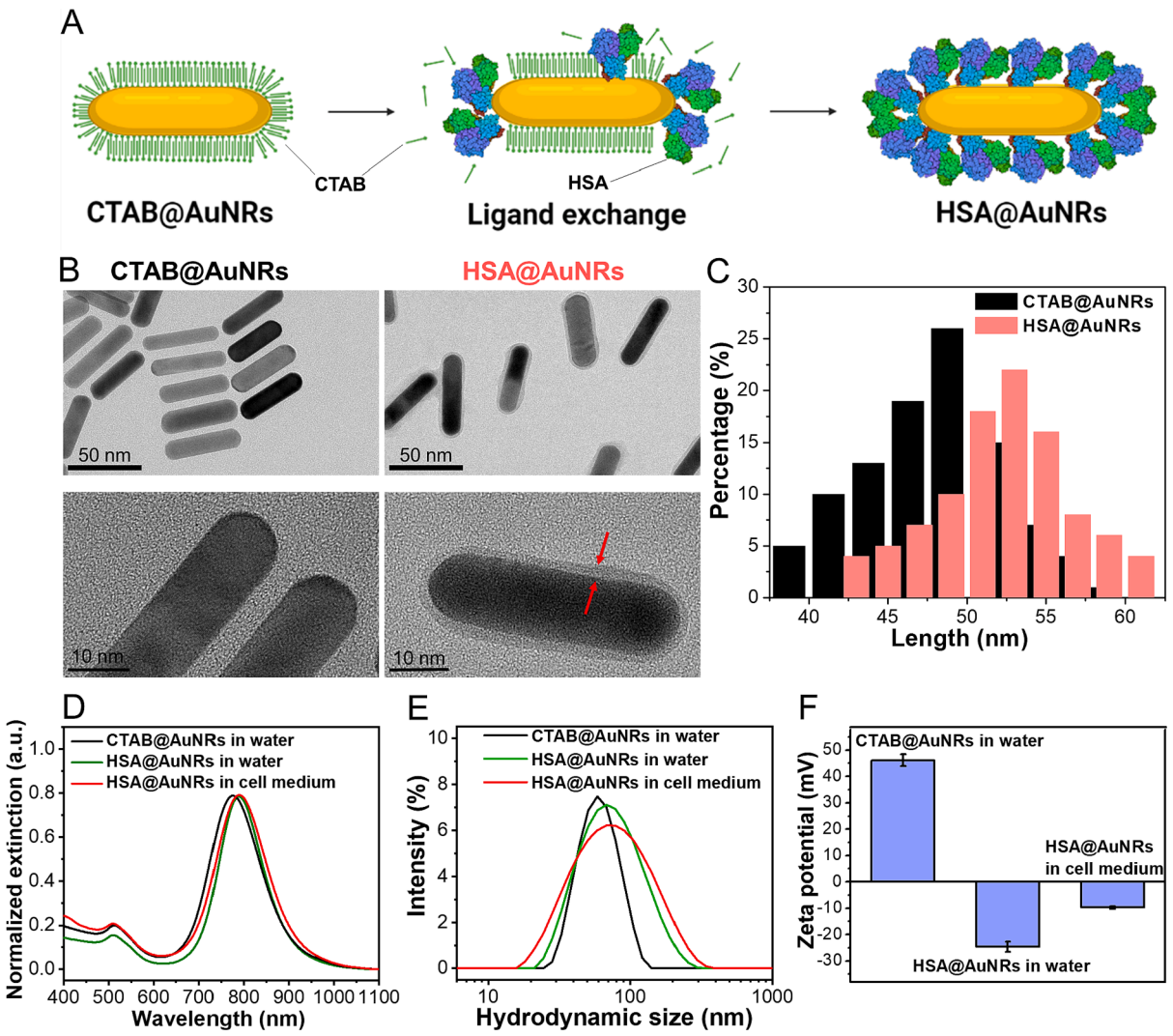

Fig. 1. (A) Diagram illustrating the ligand exchange approach to replace surfactant CTAB with HSA molecules to prepare HSA coated gold nanorods (i.e., HSA@AuNRs). (B) TEM imaging of CTAB@AuNRs and HSA@AuNRs. Red arrows indicate HSA coating surrounding the nanorod surface. (C) Statistical analysis of nanorod length in TEM images before and after HSA coating (data from 50 nanorods). (D-F) UV–vis spectra, DLS spectra and Zeta potential of CTAB@AuNRs and HSA@AuNRs in water (pH = 7.0) and cell culture medium (pH = 7.2). Error bars: SD, n = 3. (For interpretation of the references to color in this figure legend, the reader is referred to the web version of this article.)

applied biochemical assays: the XTT assay quantifies cellular mitochondrial activity as an indicator of cell viability, whereas LDH and live-dead cell assays detect a released cytoplasmic enzyme (lactate dehydrogenase, LDH) or intracellular DNA as a measure of membrane damage [45–46]. As shown in Fig. 2**A-2C**, incubation with HSA@AuNRs for 24 h induced dose-dependent effects on HAECs. It was found that 2 nanomolar (2 nM) and lower concentrations of HSA@AuNRs had negligible effect on cell viability and membrane integrity of HAECs, whereas 5 nanomolar (5 nM) and higher doses started to impair the cell viability and plasma membrane. According to these results, we selected 1 and 2 nM of HSA@AuNRs, the two concentrations without causing apparent cytotoxicity in these traditional biochemical assays, for the subsequent experiments to investigate the biophysical effect of low-dose HSA@AuNRs on HAECs.

To assess HAEC uptake of HSA@AuNRs, dark-field microscopy was utilized to visualize the cell-internalized HSA@AuNRs using the scattered light of HSA@AuNRs. As displayed in Fig. 2**D-2F**, the scattered light intensity became stronger with the increased nanorod concentration, indicating HAEC uptake of HSA@AuNRs is also dose-dependent. Importantly, the scattered light displayed “ring-like” patterns (as marked by red arrows in Fig. 2**F**) due to the accumulation of nanorods-laden vesicles around the cell’s nucleus, confirming that the nanorods were surely endocytosed into the cells, not just adhered onto the cell membrane [47–48]. Reproducible results of HAEC uptake of HSA@AuNRs investigated using dark-field imaging are presented in **Fig. S2**. According to the decrease of extinction peak in the cell supernatant, we determined that the maximal number of HSA@AuNRs is $1.8x10^5$ nanorods per cell in HAECs (**supporting information**). The large uptake amount of HSA@AuNRs by HAECs is in stark contrast with cancer cells probably due to the lack of specific HSA receptors on cancer cells [49–51]. To further investigate the endocytosis pathway of HSA@AuNRs, HAECs were first treated with an inhibitor for caveolae-mediated endocytosis (methyl-β-cyclodextrin, MβCD) [52], followed by the incubation with 2 nM HSA@AuNRs for 24 h. The dark-field images showed that pre-treating HAECs with MβCD almost abolished the cell uptake of HSA@AuNRs (Fig. 2**G**), indicating that the endocytosis pathway of HSA@AuNRs by HAECs is primarily through the caveolae-mediated endocytosis.

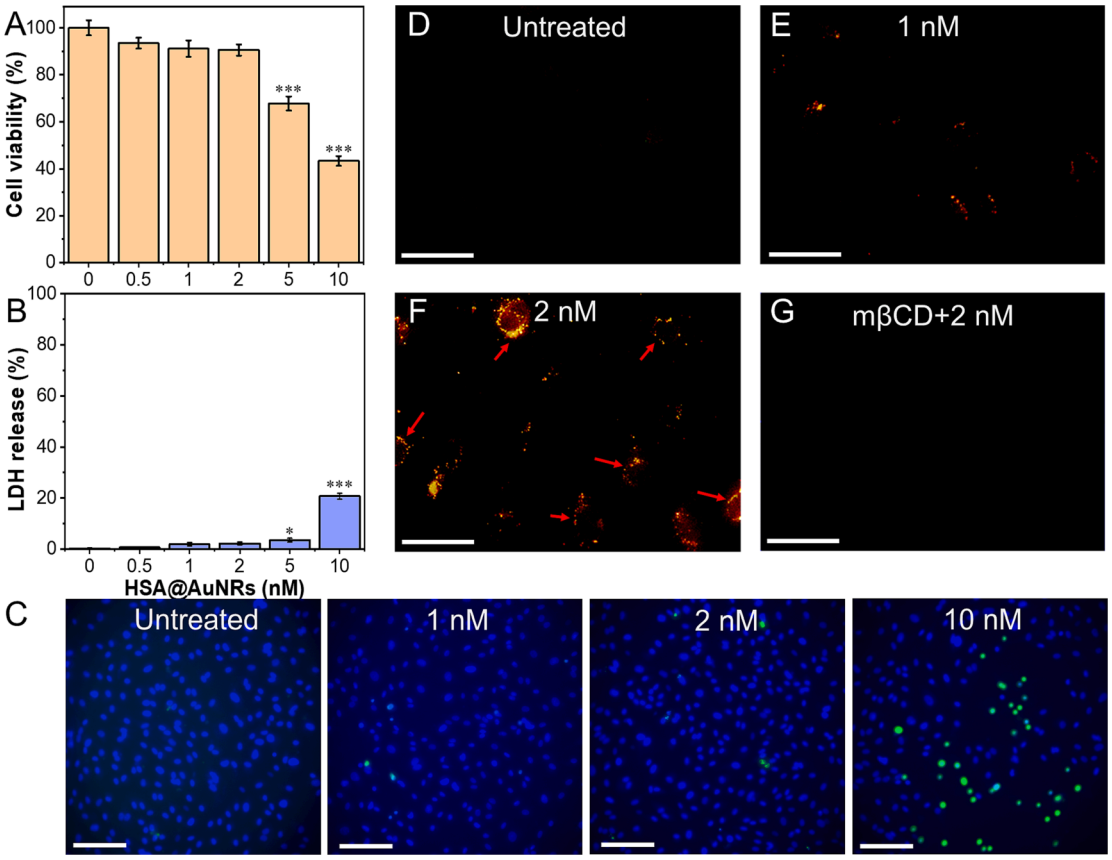

Fig. 2. (A-C) Cell viability, LDH, and live/dead cell assays assessing the dose-dependent effect of HSA@AuNRs on HAECs. The blue fluorescence indicates live cells and green fluorescence corresponds to dead cells. Error bars: SD, n = 6. One-way ANOVA, *P < 0.05, ***P < 0.001. Scale bars: 100 μm. (D-F) Dark-filed images of HAECs after 24 h incubation with 0 (untreated), 1 and 2 nM HSA@AuNRs. Red arrows in F mark the nanorods-laden intracellular vesicles surrounding the cell's nucleus. (G) Dark-filed image of MβCD pretreated HAECs after 24 h incubation with 2 nM HSA@AuNRs. Scale bars: 50 μm. (For interpretation of the references to color in this figure legend, the reader is referred to the web version of this article.)

2.3. Low-dose HSA@AuNRs increase the endothelial permeability

Next, we investigated the effect of HSA@AuNRs on the endothelial permeability of HAEC monolayers since the barrier function of vascular endothelium hinges on the permeability and integrity of endothelial monolayers. It is known that vascular endothelium acts as the door keeper to control the small and large molecules such as glucose and proteins, to cross this barrier layer [53]. To measure the endothelial permeability, HAECs were first cultivated to a confluent monolayer onto a porous *trans*-well insert, and then incubated with low-dose HSA@AuNRs, followed by adding FITC-dextran solution into the insert to quantify the FITC-dextran transport to the lower chamber (Fig. 3**A**). As shown in Fig. 3**B**, HAEC monolayers after incubating with 1 and 2 nM HSA@AuNRs for 24 h displayed ~1.7 and ~2.2 folds of increase in the FITC-dextran transport, respectively, in comparison to the untreated group, whereas pre-treating HAECs with MβCD (i.e., the inhibitor for caveolae-mediated endocytosis) eliminated the effect of 2 nM HSA@AuNRs on the FITC-dextran transport. It was found that the FITC-dextran transport elevated with the increase of nanorod incubation time. After removing un-internalized nanorods, it took another 48 h for the endothelial monolayer to return to original permeability comparable with the untreated cells (**Fig. S3**). As a control experiment, FITC-dextran transport did not change with the increase of albumin amount in the culture medium (**Fig. S4**), suggesting the multivalent effect of albumin adsorbed on HSA@AuNRs [54]. This was further validated by bovine serum albumin and polyethylene glycol coated AuNRs (BSA@AuNRs and PEG@AuNRs), where BSA@AuNRs showed similar effects on the FITC-dextran transport and PEG@AuNRs had almost no effect on the FITC-dextran transport (**Fig. S5**). Together, these results suggest that the HAEC uptake of low-dose HSA@AuNRs can increase the endothelial permeability in a dose- and time-dependent fashion, and the increased endothelial permeability occurs at the nanorod doses that conventional biochemical assays cannot identify.

To further characterize the endothelial permeability, the HAEC monolayers, with or without HSA@AuNRs treatment, were fluorescence-labelled to image the VE-cadherin (a cell junction protein shown as green fluorescence) and actin filaments (cytoskeletal actin shown as red fluorescence, Fig. 3**C**). For the untreated HAEC monolayers, we observed coherent cell junctions with VE-cadherin lining the entire cell boundary, suggesting strong cell–cell adhesion in the confluent HAEC monolayers. However, for the HAEC monolayers treated by 1 and 2 nM HSA@AuNRs, some newly formed gaps with the size of 5–20 μm were noticeable between HAECs, as marked by red-colored arrowheads. Around the gaps, the decrease of VE-cadherin led to the disrupted cell–cell adhesion in those areas. Here, 2 nM HSA@AuNRs treated monolayers exhibited larger and more gaps, compared to 1 nM HSA@AuNRs treated monolayers, consistent with the earlier data related to FITC-dextran transport. In the case of MβCD pretreated monolayers, further incubation with 1 and 2 nM HSA@AuNRs cannot cause the gap formation, suggesting the importance of nanorod endocytosis to the disrupted cell–cell adhesion (**Fig. S6**). These results were further verified through the quantitative analysis of gap area, which showed that 1 nM and 2 nM HSA@AuNRs treated monolayers displayed ~ 1% and ~ 5% of gap area, respectively (Fig. 3**D**). Apart from the loss of cell–cell adhesion, it was obvious to see that the actin structures within the cells had been changed upon the

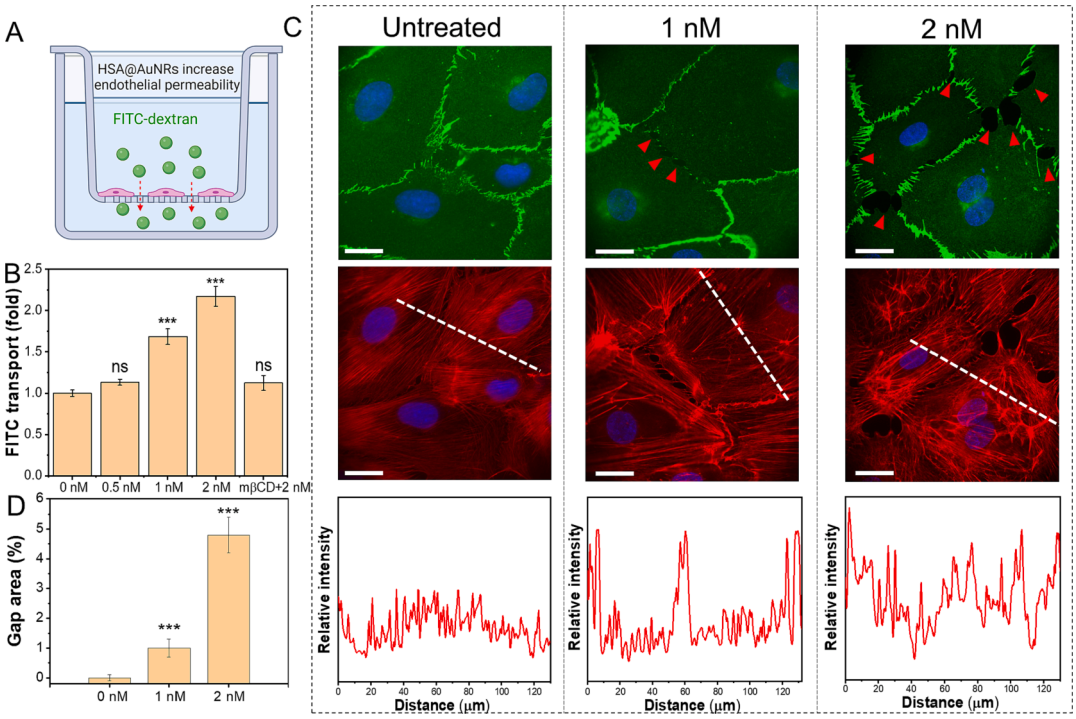

Fig. 3. (A) Schematic illustrating experimental apparatus for measuring endothelial permeability. (B) FITC-dextran transport amount across the untreated and nanorods-treated HAEC monolayers. (C) Fluorescence labelling of VE-cadherin (green) and F-actin (red) on the untreated and nanorods-treated HAEC monolayers. Red arrow heads mark the intercellular gaps formed between HAECs induced by HSA@AuNRs. Scale bars: 30 μm. White dashed lines profile the fluorescence intensity (actin density) across the HAECs. (D) Gap area analysis of HAEC monolayer based on the fluorescence images. Error bars: SD, n = 3. One-way ANOVA, ***P < 0.001. (For interpretation of the references to color in this figure legend, the reader is referred to the web version of this article.)

treatment of HSA@AuNRs. The untreated HAEC monolayers possessed evenly distributed, thin actin filaments along the cell length. In contrast, HSA@AuNRs treated monolayers showed unevenly distributed actin filaments with the appearance of thicker radial actin bundles. With the increase of nanorods concentration, the number of radial actin bundles dramatically increased, especially in the 2 nM HSA@AuNRs treated groups. Reproducible results of VE-cadherin and actin imaging on HAEC monolayers are summarized in **Fig. S7-S9**. Considering the critical roles of cytoskeletal actin in the modulation of intracellular tension and cell–cell adhesion [55–56], it is reasonable to believe these radial actin bundles generated the contraction force in the HAECs and pulled the cell junction proteins (e.g., VE-cadherins) inside the cells, thus leading to the loss of cell–cell adhesion, formation of intercellular gaps, and increased endothelial permeability.

2.4. Low-dose HSA@AuNRs alter the actin structure and cell morphology of single HAECs

To better examine the effect of HSA@AuNRs on the cytoskeletal actin and cell morphology of HAECs, a nanoscale tool, atomic force microscopy-based nanomechanical imaging, was utilized to characterize single HAECs. This live-cell imaging technique uses a spherical probe to scan through the cell in a temperature-controlled culture medium (Fig. 4**A**), collects a force-indentation curve at each pixel, and simultaneously generates height, surface topography, and elastic modulus images based on Hertz model (Fig. 4**B**) [57–59]. By correlating these images, the actin structures within the cell's upper layer are identifiable as they are typically stiffer than the rest of cells [60–62]. As shown in Fig. 4**C**, the untreated HAECs possessed an elongated cell morphology with dense, well-aligned actin filaments paralleled to the cell length. By correlating the images in topography and modulus channels, we observed precise co-localization between higher topography and stiffer areas (marked by green arrows), which indicated the locations of actin filaments. However, after treated by HSA@AuNRs, the cell shape became circular, meanwhile the cell's aspect ratio reduced from ~ 2.0 (untreated) to ~ 1.6 (1 nM nanorods treated) and further to ~ 1.2 (2 nM nanorods treated) (Fig. 4**D**). More importantly, with the increase of nanorod concentration, the well-aligned actin filaments gradually disappeared, while the thicker, radial actin bundles became dominant structures (marked by red arrows), consistent with our previous observations on HAEC monolayers.

The cytoskeletal actin and cell morphology changes of HAECs were further validated by another nanoscale tool: direct stochastic optical reconstruction microscopy (dSTORM). Instead of focusing on actin structures at the upper layer of the cell, dSTORM adopts total internal reflection fluorescence (TIRF) mode that resolves actin structures at the bottom layer of the cell (Fig. 5**A**). Importantly, dSTORM offers drastically improved imaging resolution compared to the traditional wide-field microscopy by stochastically activating individual fluorophores and an image reconstruction process (Fig. 5**B**), which allows precise quantification of actin orientation altered by the HSA@AuNRs treatment. As shown in Fig. 5**C**, HAECs treated by HSA@AuNRs gradually lost the parallel actin filaments and increased radial stress fibers, as confirmed by the quantitative analysis of actin orientations (Fig. 5**D**) showing the wider distribution of actin orientations/angles. Reproducible results of AFM and dSTORM images of single HAECs are presented in **Figs. S10-S15**. Together, AFM and dSTORM demonstrate that the low-dose HSA@AuNRs cause the cytoskeletal and morphological changes of HAECs in a dose-dependent manner. Notably, the appearance of radial actin stress fibers upon the nanorod treatments suggests the actin-mediated radial contraction of individual cells, which reduces the stability of cell–cell adhesion and endothelial integrity [63–64].

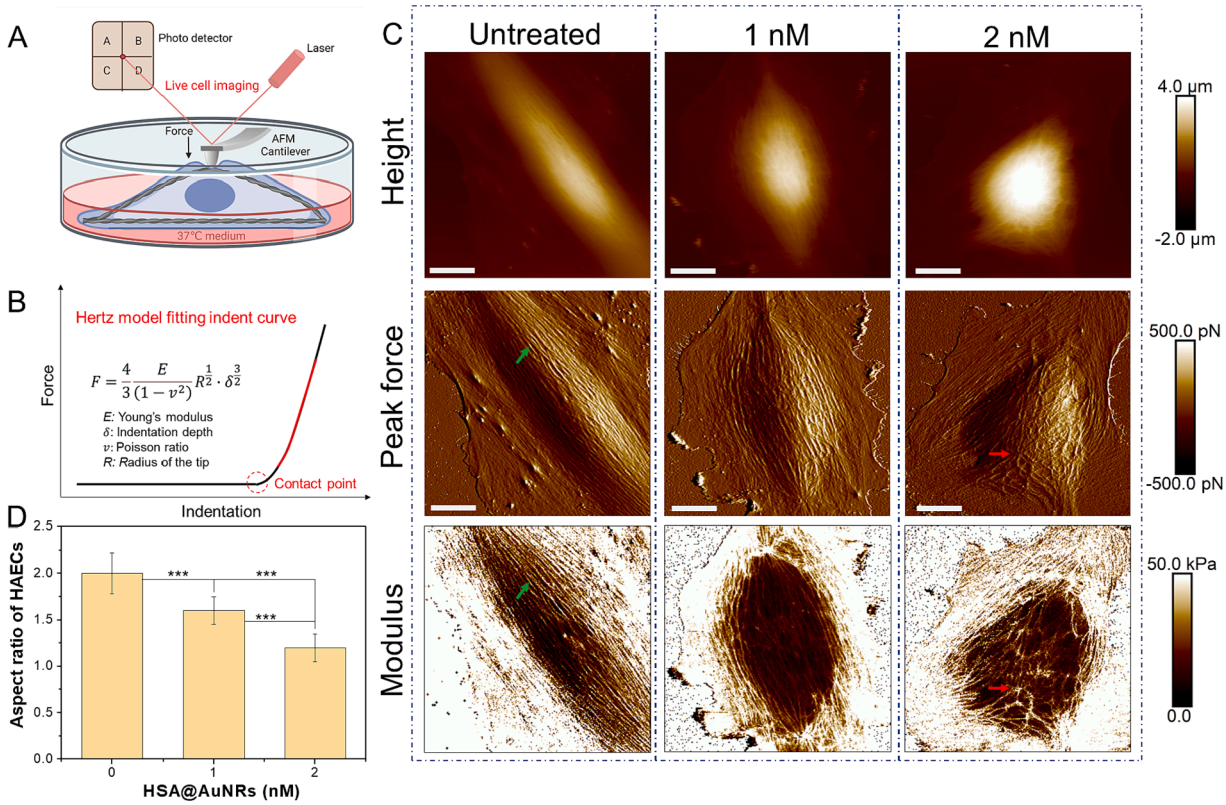

Fig. 4. (A) Schematic illustrating the concept of nanomechanical imaging of live cells. (B) Hertz model used for generating Young's modulus from a force-indentation curve. (C) Nanomechanical images of untreated and nanorods-treated single HAECs. Three image channels including height, surface topography (Peak force), and modulus images of the same cells were collected simultaneously. Green arrows mark the well-aligned actin filaments on untreated HAECs along the cell length. Red arrows mark the thick, radial actin stress fibers on 2 nM nanorods-treated HAECs. Scale bars: 20 μm. (D) Aspect ratio of single cells after different treatments. Error bars: SD, n = 20. One-way ANOVA, ***P < 0.001. (For interpretation of the references to color in this figure legend, the reader is referred to the web version of this article.)

2.5. Molecular mechanism of actin contraction induced by low-dose HSA@AuNRs

Finally, we sought to understand the molecular mechanism by which low-dose HSA@AuNRs caused the contraction of cytoskeletal actin within HAECs. Previous studies have suggested a close relationship between caveolae-mediated endocytosis and calcium influx in endothelial cells, due to the important role of caveolin-1 in regulating the assembly of calcium-permeable transient receptor potential canonical (TRPC) channels on the cell membrane and activating the subsequent calcium influx pathway [65–67]. Therefore, the caveola formation facilitates the entry of calcium ions in endothelial cells. Interestingly, albumin specifically binds to an albumin-binding receptor, Gp60, localized on the caveolar plasma membrane and therefore activates caveolae-mediated endocytosis of albumin in endothelial cells [68–69]. Inspired by these findings and our earlier results related to endocytosis pathway of HSA@AuNRs, we proposed the following hypothesis as illustrated in Fig. 6**A**: initially, the caveolae-mediated endocytosis of albumin-coated gold nanorods, mediated by the binding of albumin and Gp60, will trigger the calcium influx in HAECs. Next, the increased intracellular calcium ions will bind to a calcium binding protein, calmodulin (step 1), and the calcium-calmodulin complex will further bind/activate myosin light-chain kinase (MLCK) (step 2), which will trigger the phosphorylation of myosin light-chain (MLC to p-MLC, step 3). Finally, the p-MLC will enable the actomyosin (actin-myosin) interaction that generates the contraction force to pull the VE-cadherin apart (step 4), leading to the loss of cell–cell adhesion and enhanced endothelial permeability.

To test our hypothesis, we first measured the intracellular calcium ions in the HAECs using a fluorescent-based, calcium ion-sensing assay. The fluorescence images and quantification of fluorescence intensity of individual cells revealed that treating HAECs with 1 and 2 nM HSA@AuNRs caused ~1.5 and ~2 folds of increase in the intracellular calcium ions, respectively, in comparison with untreated HAECs (Fig. 6**B-6C**). We believe the increase of intracellular calcium ions here is due to the activation of TRPC channels since pre-treating HAECs with a well-established TRPC inhibitor (Pico145) [70] can attenuate the calcium influx caused by the HSA@AuNRs (**Fig. S16**). These results were in well accordance with the earlier nanorods uptake and FITC-dextran transport results (Fig. 2**D-2F**, Fig. 3**B**). Therefore, it can be concluded that the caveolae-mediated endocytosis of HSA@AuNRs triggered the calcium influx in HAECs in a dose-dependent manner. Next, we examined the essential protein markers involved in the calcium influx pathway using the Western blot method (Fig. 6**D**). We found that the amount of membrane Gp60 reduced with the increase of HSA@AuNRs doses (Fig. 6**E**), suggesting that endocytosis of HSA@AuNRs was initiated by the binding between albumin on the nanorods and Gp60 on the caveolar plasma membrane, which caused the depletion of membrane Gp60 to intracellular degradative vesicles, as proved by the earlier nanorods localization analysis in the dark-field images (Fig. 2**F**). More importantly, the Western blots also showed that the phosphorylation level of myosin light-chain (i.e., p-MLC), elevated along the increase of HSA@AuNRs concentration (Fig. 6**F-6G**), consistent with the trend of calcium ion increase (Fig. 6**C**). Considering the vital role of p-MLC in the regulation of actomyosin contractility [71–72], these data clearly revealed that the endocytosis of HSA@AuNRs caused the calcium influx, and further trigged the cell contraction by activating the actomyosin contraction machine. Here, it should be noted that this actin-changing mechanism induced by HSA@AuNRs is quite distinct from the

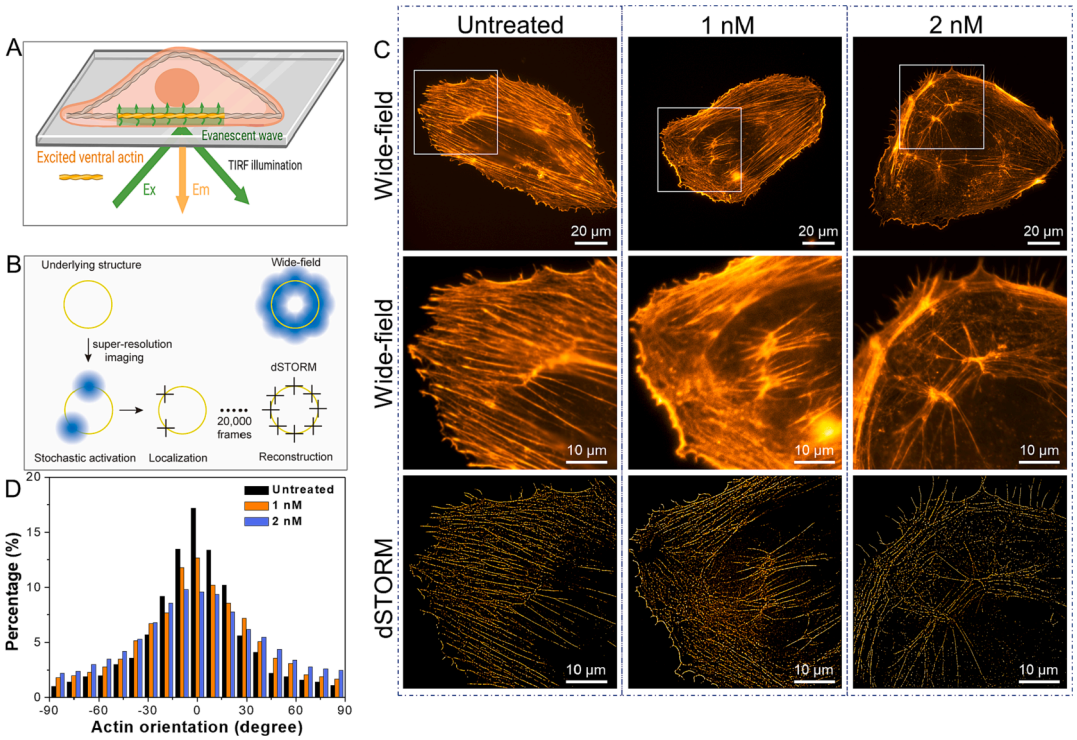

Fig. 5. (A) Diagram showing TIRF illumination of cytoskeletal actin at the bottom layer of single cells. (B) Schematic illustrating the workflow of dSTORM imaging. (C) Wide-field versus dSTORM imaging of cytoskeletal actin in untreated and nanorods-treated single HAECs. (D) Actin fiber orientation in untreated and nanorods-treated single HAECs.

previously studies stating that the actin structures were altered owing to the elevation of reactive oxygen species (ROS) induced by the uptake of metal nanoparticles [73–74], as our ROS assays confirmed that the uptake of HSA@AuNRs did not cause the increase of ROS level in HAECs (**Fig. S17**). This mechanism is also different from earlier studies on microvascular endothelial cells, where the metallic nanoparticles directly contacted and interacted with VE-cadherin in cell junctions, causing the actin remodeling [75–76]. Together, these results elucidate the molecular mechanism of actin contraction induced by low-dose HSA@AuNRs: the binding between HSA@AuNRs and Gp60 located at caveolar membrane of HAECs triggers the caveolae-mediated endocytosis of HSA@AuNRs, causes the calcium influx in HAECs, and further activates the myosin light-chain phosphorylation, thus leading to the actomyosin contraction and enhanced endothelial permeability.

3. Conclusion

This work demonstrated that the cell uptake of albumin-coated gold nanorods (HSA@AuNRs), even at the doses when membrane integrity and cell viability remained unchanged, can induce the formation of intercellular gaps between human aortic endothelial cells (HAECs). By examining the HSA@AuNRs-treated HAECs at the monolayer and single cell levels, we found that the formation of intercellular gaps was owing to the loss of cell–cell adhesion, along with the altered cell morphology and cytoskeletal actin structures. In particular, the appearance of radial actin stress fibers suggested the increased actomyosin contractility, which generated contraction force to pull endothelial cells apart. Further mechanistic study at the molecular level demonstrated that the caveolae-mediated endocytosis of HSA@AuNRs, mediated by specific binding between albumin and its membrane receptor (Gp60), caused the calcium influx in HAECs, and further activated the myosin light-chain phosphorylation, leading to the actomyosin contraction and enhanced endothelial permeability. Together, these results reveal a potential adverse effect of low-dose albumin-coated gold nanorods on human health, as the endothelial integrity/dysfunction play important roles in various physiological/pathological conditions, especially in the cardiovascular system. It should be noted that the in vitro data cannot extrapolate the *in vivo* scenario where blood flow will serve as an important factor to determine the nanoparticle-endothelium interaction. However, the in vitro studies here can provide important insights into the mechanism of intercellular gap formation and suggest the limitations of conventional biochemical assays when conducting in vitro tests. On the other hand, this work also suggests a possible way to modulate the endothelial permeability to serve the human health in a beneficial manner [77]. For example, an on-going study in our group is to design gold nanoparticles combined with laser treatment to enhance the tumor endothelial permeability, promoting the delivery of anticancer drugs and nanoparticles into the tumor through the paracellular transport across endothelium, especially for certain tumors without an innate leaky endothelial structure.

4. Experimental

Materials: Hexadecyltrimetylammonium bromide (CTAB, ≥98%), gold (III) chloride trihydrate (≥99.9%), silver nitrate (≥99%), sodium borohydride (≥99%), L-ascorbic acid (≥99%), methyl-beta-cyclodextrin (≥98%), thiolated polyethylene glycol (PEG) (2 kDa), and 40 kDa dextran conjugated with FITC were purchased from Sigma. Human serum albumin, bovine serum albumin (BSA), paraformaldehyde, DPBS, PBS, and Pierce BCA Protein Assay Kit were acquired from Thermal Fisher. Pico145 was purchased from GLPBIO (>98.5%). Human aortic endothelial cell line, basal culture medium, and growth kit-VEGF were obtained from ATCC.

Gold nanorods synthesis: 0.6 ml of 10 mM ice-cold sodium borohydride was mixed with 9.75 ml of 100 mM CTAB, followed by adding with 0.25 ml of 10 mM gold (III) chloride trihydrate. The mixed solution was vigorously mixed until color turned from yellowish to brownish (seed solution). To grow nanorods, 95 ml of 100 mM CTAB was added

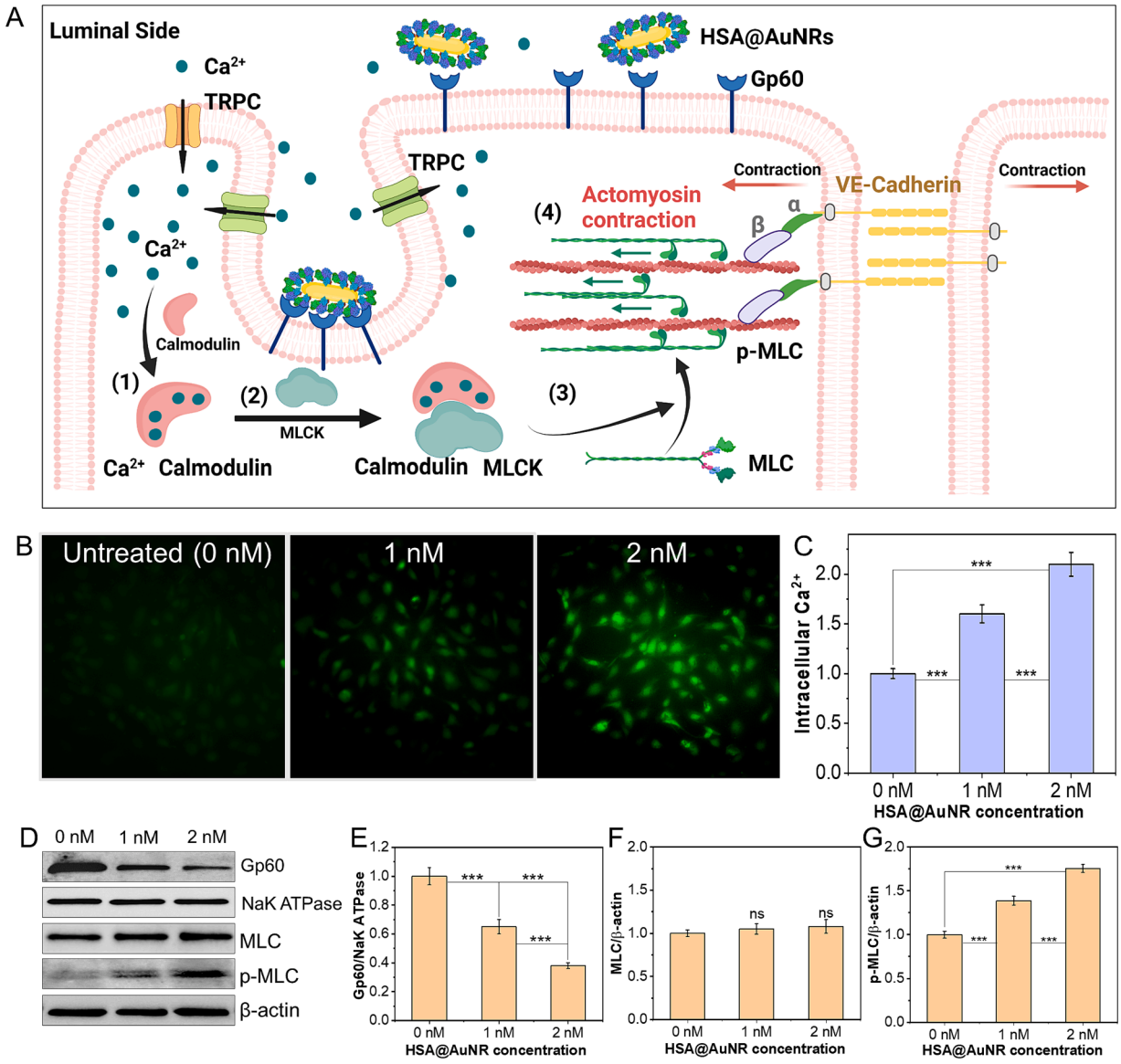

Fig. 6. (A) Schematic illustrating the molecular mechanism of how the HAEC uptake of HSA@AuNRs causes the actomyosin contraction, leading to the formation of intercellular gaps and enhanced endothelial permeability. (B-C) Intracellular calcium levels of untreated and nanorods-treated HAECs. (D-G) Western blot analyses of membrane Gp60, and cytoplasmic MLC and MLC phosphorylation (p-MLC) of untreated and nanorods-treated HAECs. NaK ATPase and β-actin serve as house-keeping proteins for membrane Gp60 and cytoplasmic proteins. Error bars: SD. n = 3. One-way ANOVA, ***P < 0.001.

with 1 ml of 10 mM silver nitrate, 5 ml of 10 mM gold (III) chloride trihydrate solution, and 0.55 ml of 100 mM L-ascorbic acid in a sequential manner. The mixture was gently stirred to colorless, added with 0.12 ml of seed solution, and left undisturbed to grow nanorods. After 16 h, the nanorods were washed in deionized H_2O using centrifugation for removing unreacted chemicals and excess surfactant.

Preparation of HSA-coated AuNRs (HSA@AuNRs): HSA@AuNRs were prepared using a ligand exchange approach established in our group [41]. Highly concentrated AuNRs were slowly pipetted to HSA solution (5 mg/mL, pH = 7) in a centrifuge tube under the sonication within 20 min. After this process, the nanorods were centrifuged down and the HSA supernatant was removed. Then the nanorods were re-dispersed in HSA solution (0.5 mg/mL, pH = 12) and left for 12 h. Finally, the nanorods were washed with pH = 11 H_2O and re-dispersed in PBS buffer (pH = 7.2) for future experiment. The BSA-coated AuNRs (HSA@AuNRs) was prepared using the similar protocol. For the PEG-coated AuNRs (PEG@AuNRs), highly concentrated AuNRs were slowly pipetted to PEG solution (1 μM) and stirred overnight at room temperature. Then the nanorods were washed with pH = 7 H_2O and re-dispersed in pH = 7 H_2O for future experiment.

Nanorods characterization: Shimadzu UV1900 spectrometer, Malvern Zetasizer Nano-system, and JEOL JEM2100 transmission electron microscopy (200 keV) were applied to characterize gold nanorods and HSA coating.

Cytotoxicity assays: Three types of cytotoxicity assays were carried out, including XTT, LDH, and live/dead staining assays. 8,000–10,000 cells were seeded to each well of a 96-well plate and left in cell incubator for overnight. After removing old medium, new medium with HSA@AuNRs was added and left for 24 h. XTT assay was performed following a protocol provided by the XTT Cell Viability Assay Kit (CyQUANT™, Thermo Fisher). LDH assay was performed following a protocol provided by the LDH Cytotoxicity Assay Kit (CyQUANT™, Thermo Fisher). Live/dead staining assay was performed using a ReadyProbes™ Cell Viability Imaging Kit (Thermo Fisher).

Dark-field imaging: 10,000 HAECs were seeded onto a coverslip, and then immersed into culture medium containing nanorods. For

methyl-beta-cyclodextrin group, the HAECs on coverslip were first treated with 4 mM methyl-beta-cyclodextrin in culture medium for 1 h, rinsed by DPBS, and then immersed into culture medium containing nanorods. After 24 h of immersion with nanorods, the coverslips were washed by DPBS and fixed with 4% paraformaldehyde for 10 min for the subsequent dark-field imaging.

Endothelial permeability assay: HAECs were cultivated to a 100% confluent monolayer onto a Corning *trans*-well insert with 0.4 μm pore size. After incubating the monolayer with culture medium containing nanorods for different time periods, the cell medium was replaced with dextran-FITC solution. After a 30 min wait, the transport of dextran-FITC to lower chamber of the *trans*-well was quantified by a fluorescence plate reader (Ex/Em = 495/516 nm).

Fluorescence labelling of VE-cadherin and F-actin: HAECs were cultivated to a 100% confluent monolayer onto an imaging dish with a diameter of 50 mm. After treating by nanorods, the cells were processed by the following steps: washing by DPBS, fixing with 4% paraformaldehyde for 10 min and permeabilizing with 0.1% Triton-X 100 for 10 min. To label VE-cadherin, the cells were then incubated with BlockAid blocking solution for 1 h, VE-cadherin antibody (CST Inc.) for 12 h, and secondary antibody (AlexaFluor 488, CST Inc.) for 1 h in a sequential manner. To label F-actin, ActinRed ReadyProbes 555 (Thermo Fisher) was used.

AFM Imaging: Bruker's BioScope Resolve AFM was applied to image single, live HAECs at 37 °C in imaging medium. PFQNM-LC-A-CAL probes were used for nanomechanical imaging, with 300–600 nm oscillation amplitude and 0.8–1 nN set point. Single cell was scanned using a frequency of 0.12 Hz and 256x256 pixels. This probe was selected because it has a dull geometry (65 nm in radius), minimizing the damage to cells, and it also has a 15 μm probe height, avoiding the contact of cantilever with cells. AFM images and indentation curves were analyzed using the NanoScope Analysis (v1.9, Bruker). The calculation of cell aspect ratio is based on the length of cells divided by the width at 1/2 of length of the cells (n = 10).

dSTORM imaging: HAECs, with or without nanorods treatment, were processed using a similar protocol as fluorescence labelling of F-actin except AlexaFluor 568 phalloidin (Thermo Fisher) was used for F-actin labelling here. The detailed procedure for dSTORM imaging was documented in our previous paper [78]. Different from conventional epifluorescence microscopy, dSTORM implements a total internal reflection illumination, making sure only fluorophores 100–200 nm above the cover glass are efficiently excited, thereby eliminating the background fluorescence outside the focal plane. The image was generated and analyzed using ThunderSTORM and ImageJ.

Intracellular calcium and ROS assays: HAECs seeded in an imaging dish were treated with cell culture medium containing 0, 1 or 2 nM HSA@AuNRs for 24 h. Then the intracellular calcium levels were determined using a Screen Quest™ Fluo-8 No Wash Calcium Assay Kit (AAT Bioquest). The ROS levels were measured in a similar manner, where a cell-permeable fluorescence probe, 2′,7′-dichlorodihydrofluorescein diacetate (Sigma) was used for probing ROS. A fluorescence plate reader (Ex/Em = 495/516 nm) was used to quantify the calcium and ROS. The calcium and ROS levels of the nanorods treated HAECs were normalized to the levels in the untreated HAECs.

Western blot: HAECs were lysed 0.5 h following the nanorods treatment to track the early signaling. For membrane Gp60, Mem-PER™ Plus Membrane Protein Extraction Kit (Thermo Fisher) was applied to lyse HAECs. The same protein amount was loaded to a 4–20% gel based on the quantification using a bicinchoninic acid assay (Thermo Fisher). Then the gels were transferred to Nitrocellulose membrane and processed by EveryBlot blocking buffer (Bio-Rad). A Gp60 antibody from mouse (sc-58156, Santa Cruz) was used as the primary antibody to stain the blots for 12 h with shaking. A HRP conjugated goat anti-mouse IgG antibody was selected as the secondary antibody. For MLC and p-MLC proteins, RIPA buffer was used for cell lysis. The gel running and transfer processes followed the protocols mentioned before, except MLC, p-MLC, and β-actin antibodies were used as the primary antibodies (3672S, 3671S, 4967S produced from rabbit, CST Inc.). A HRP conjugated goat anti-rabbit IgG was selected as the secondary antibody. For imaging blots, Chemi-Doc imaging system from Bio-Rad was used.

CRediT authorship contribution statement

Zhengqiang Li: Methodology, Formal analysis, Investigation, Validation, Writing – original draft, Visualization. **Jinyuan Liu:** Methodology, Formal analysis, Investigation, Validation, Visualization. **Katherine Ballard:** Investigation, Validation, Visualization. **Chao Liang:** Conceptualization, Methodology, Writing – review & editing. **Congzhou Wang:** Conceptualization, Validation, Funding acquisition, Supervision, Writing – review & editing, Project administration.

Declaration of Competing Interest

The authors declare that they have no known competing financial interests or personal relationships that could have appeared to influence the work reported in this paper.

Data availability

Data will be made available on request.

Acknowledgements

The authors thank the support from the National Science Foundation CAREER Award (Award number: 2143972).

Appendix A. Supplementary material

Supplementary data to this article can be found online at https://doi.org/10.1016/j.jcis.2023.06.154.

References

[1] A. Kroll, M.H. Pillukat, D. Hahn, J. Schnekenburger, Current in vitro methods in nanoparticle risk assessment: Limitations and challenges, Eur. J. Pharm. Biopharm. 72 (2) (2009) 370–377.
[2] N. Lewinski, V. Colvin, R. Drezek, Cytotoxicity of nanoparticles, Small 4 (1) (2008) 26–49.
[3] B. Kong, J.H. Seog, L.M. Graham, S.B. Lee, Experimental considerations on the cytotoxicity of nanoparticles, Nanomedicine 6 (5) (2011) 929–941.
[4] A.M. Alkilany, C.J. Murphy, Toxicity and cellular uptake of gold nanoparticles: what we have learned so far? J. Nanoparticle Res.: Interdiscipl. Forum Nanoscale Sci. Technol. 12 (7) (2010) 2313–2333.
[5] The dose makes the poison. Nat. Nanotechnol. 6 (6) (2011) 329–329.
[6] X. Ma, R. Hartmann, D. Jimenez de Aberasturi, F. Yang, S.J.H. Soenen, B. B. Manshian, J. Franz, D. Valdeperez, B. Pelaz, N. Feliu, N. Hampp, C. Riethmüller, H. Vieker, N. Frese, A. Gölzhäuser, M. Simonich, R.L. Tanguay, X.-J. Liang, W. J. Parak, Colloidal gold nanoparticles induce changes in cellular and subcellular morphology, ACS Nano 11 (8) (2017) 7807–7820.
[7] M.I. Setyawati, C. Sevencan, B.H. Bay, J. Xie, Y. Zhang, P. Demokritou, D.T. Leong, Nano-TiO2 drives epithelial-mesenchymal transition in intestinal epithelial cancer cells, Small 14 (30) (2018) 1800922.
[8] S.J. Soenen, B. Manshian, J.M. Montenegro, F. Amin, B. Meermann, T. Thiron, M. Cornelissen, F. Vanhaecke, S. Doak, W.J. Parak, S. De Smedt, K. Braeckmans, Cytotoxic effects of gold nanoparticles: a multiparametric study, ACS Nano 6 (7) (2012) 5767–5783.
[9] Y.-L. Wu, N. Putcha, K.W. Ng, D.T. Leong, C.T. Lim, S.C.J. Loo, X. Chen, Biophysical responses upon the interaction of nanomaterials with cellular interfaces, Acc. Chem. Res. 46 (3) (2013) 782–791.
[10] M.A.I. Rasel, S. Singh, T.D. Nguyen, I.O. Afara, Y. Gu, Impact of nanoparticle uptake on the biophysical properties of cell for biomedical engineering applications, Sci. Rep. 9 (1) (2019) 5859.
[11] D. Septiadi, F. Crippa, T.L. Moore, B. Rothen-Rutishauser, A. Petri-Fink, Nanoparticle-Cell Interaction: A Cell Mechanics Perspective, Adv. Mater. 30 (19) (2018) 1704463.
[12] M.R.K. Ali, M.A. Rahman, Y. Wu, T. Han, X. Peng, M.A. Mackey, D. Wang, H. J. Shin, Z.G. Chen, H. Xiao, R. Wu, Y. Tang, D.M. Shin, M.A. El-Sayed, Efficacy, long-term toxicity, and mechanistic studies of gold nanorods photothermal therapy of cancer in xenograft mice, Proc. Natl. Acad. Sci. 114 (15) (2017) E3110–E3118.

[13] X. Li, L. Xing, K. Zheng, P. Wei, L. Du, M. Shen, X. Shi, Formation of gold nanostar-coated hollow mesoporous silica for tumor multimodality imaging and photothermal therapy, ACS Appl. Mater. Interfaces 9 (7) (2017) 5817–5827.
[14] S. Lu, X. Li, J. Zhang, C. Peng, M. Shen, X. Shi, Dendrimer-stabilized gold nanoflowers embedded with ultrasmall iron oxide nanoparticles for multimode imaging-guided combination therapy of tumors, Adv. Sci. 5 (12) (2018) 1801612.
[15] M. You, P. Jia, X. He, Z. Wang, S. Feng, Y. Ren, Z. Li, L. Cao, B. Gao, C. Yao, S. Singamaneni, F. Xu, Quantifying and Adjusting Plasmon-Driven Nano-Localized Temperature Field around Gold Nanorods for Nucleic Acids Amplification, Small Methods 5 (5) (2021) 2001254.
[16] C. Liang, J. Luan, Z. Wang, Q. Jiang, R. Gupta, S. Cao, K.-K. Liu, J.J. Morrissey, E. D. Kharasch, R.R. Naik, S. Singamaneni, Gold Nanorod Size-Dependent Fluorescence Enhancement for Ultrasensitive Fluoroimmunoassays, ACS Appl. Mater. Interfaces 13 (9) (2021) 11414–11423.
[17] Z. Yin, H. Guo, Y. Li, J. Chiu, L. Tian, Ultrastable Plasmonic Bioink for Printable Point-Of-Care Biosensors, ACS Appl. Mater. Interfaces 12 (32) (2020) 35977–35985.
[18] S. Tadepalli, J. Yim, K. Madireddi, J. Luan, R.R. Naik, S. Singamaneni, Gold Nanorod-Mediated Photothermal Enhancement of the Biocatalytic Activity of a Polymer-Encapsulated Enzyme, Chem. Mater. 29 (15) (2017) 6308–6314.
[19] H.S. Han, K.Y. Choi, Advances in Nanomaterial-Mediated Photothermal Cancer Therapies: Toward Clinical Applications, Biomedicines 9 (3) (2021).
[20] A.M. Alkilany, P.K. Nagaria, C.R. Hexel, T.J. Shaw, C.J. Murphy, M.D. Wyatt, Cellular uptake and cytotoxicity of gold nanorods: molecular origin of cytotoxicity and surface effects, Small 5 (6) (2009) 701–708.
[21] X. Shi, H.L. Perry, J.D.E.T. Wilton-Ely, Strategies for the functionalisation of gold nanorods to reduce toxicity and aid clinical translation, Nanotheranostics 5 (2) (2021) 155–165.
[22] J.S. Suk, Q. Xu, N. Kim, J. Hanes, L.M. Ensign, PEGylation as a strategy for improving nanoparticle-based drug and gene delivery, Adv. Drug Deliv. Rev. 99 (Pt A) (2016) 28–51.
[23] Q. Dai, C. Walkey, W.C.W. Chan, Polyethylene Glycol Backfilling Mitigates the Negative Impact of the Protein Corona on Nanoparticle Cell Targeting, Angew. Chem. Int. Ed. 53 (20) (2014) 5093–5096.
[24] S. Chen, L. Li, C. Zhao, J. Zheng, Surface hydration: Principles and applications toward low-fouling/nonfouling biomaterials, Polymer 51 (23) (2010) 5283–5293.
[25] B.-M. Chen, T.-L. Cheng, S.R. Roffler, Polyethylene Glycol Immunogenicity: Theoretical, Clinical, and Practical Aspects of Anti-Polyethylene Glycol Antibodies, ACS Nano 15 (9) (2021) 14022–14048.
[26] P. Zhang, F. Sun, S. Liu, S. Jiang, Anti-PEG antibodies in the clinic: Current issues and beyond PEGylation, J. Control. Release 244 (2016) 184–193.
[27] H. Hyun, J. Park, K. Willis, J.E. Park, L.T. Lyle, W. Lee, Y. Yeo, Surface modification of polymer nanoparticles with native albumin for enhancing drug delivery to solid tumors, Biomaterials 180 (2018) 206–224.
[28] T. Takeuchi, Y. Kitayama, R. Sasao, T. Yamada, K. Toh, Y. Matsumoto, K. Kataoka, Molecularly imprinted nanogels acquire stealth in situ by cloaking themselves with native dysopsonic proteins, Angewandte Chem. (International ed. in English) 56 (25) (2017) 7088–7092.
[29] A. Spada, J. Emami, J.A. Tuszynski, A. Lavasanifar, The Uniqueness of Albumin as a Carrier in Nanodrug Delivery, Mol. Pharm. 18 (5) (2021) 1862–1894.
[30] E.N. Hoogenboezem, C.L. Duvall, Harnessing albumin as a carrier for cancer therapies, Adv. Drug Deliv. Rev. 130 (2018) 73–89.
[31] W. Poon, Y.-N. Zhang, B. Ouyang, B.R. Kingston, J.L.Y. Wu, S. Wilhelm, W.C. W. Chan, Elimination Pathways of Nanoparticles, ACS Nano 13 (5) (2019) 5785–5798.
[32] Y. Wu, T. Yu, T.A. Gilbertson, A. Zhou, H. Xu, K.T. Nguyen, Biophysical Assessment of Single Cell Cytotoxicity: Diesel Exhaust Particle-Treated Human Aortic Endothelial Cells, PLoS One 7 (5) (2012) e36885.
[33] V.G. Walker, Z. Li, T. Hulderman, D. Schwegler-Berry, M.L. Kashon, P. P. Simeonova, Potential in vitro effects of carbon nanotubes on human aortic endothelial cells, Toxicol. Appl. Pharmacol. 236 (3) (2009) 319–328.
[34] N. Miyazawa, M. Abe, T. Souma, M. Tanemoto, T. Abe, M. Nakayama, S. Ito, Methylglyoxal augments intracellular oxidative stress in human aortic endothelial cells, Free Radic. Res. 44 (1) (2010) 101–107.
[35] H.-J. Sun, Z.-Y. Wu, X.-W. Nie, J.-S. Bian, Role of Endothelial Dysfunction in Cardiovascular Diseases: The Link Between Inflammation and Hydrogen Sulfide, Front. Pharmacol. 10 (2020).
[36] C. Michiels, Endothelial cell functions, J. Cell. Physiol. 196 (3) (2003) 430–443.
[37] L. Claesson-Welsh, E. Dejana, D.M. McDonald, Permeability of the Endothelial Barrier: Identifying and Reconciling Controversies, Trends Mol Med 27 (4) (2021) 314–331.
[38] B. Nikoobakht, M.A. El-Sayed, Preparation and Growth Mechanism of Gold Nanorods (NRs) Using Seed-Mediated Growth Method, Chem. Mater. 15 (10) (2003) 1957–1962.
[39] T.K. Sau, C.J. Murphy, Seeded High Yield Synthesis of Short Au Nanorods in Aqueous Solution, Langmuir 20 (15) (2004) 6414–6420.
[40] U. Mogera, H. Guo, M. Namkoong, M.S. Rahman, T. Nguyen, L. Tian, Wearable plasmonic paper–based microfluidics for continuous sweat analysis, Sci. Adv. 8 (12) (2022) eabn1736.
[41] J. Liu, L. Kang, I. Ratnayake, P. Ahrenkiel, S. Smith, C. Wang, Targeting cancer cell adhesion molecule, CD146, with low-dose gold nanorods and mild hyperthermia disrupts actin cytoskeleton and cancer cell migration, J. Colloid Interface Sci. 601 (2021) 556–569.
[42] M. Tebbe, C. Kuttner, M. Männel, A. Fery, M. Chanana, Colloidally Stable and Surfactant-Free Protein-Coated Gold Nanorods in Biological Media, ACS Appl. Mater. Interfaces 7 (10) (2015) 5984–5991.
[43] C. Hanske, M. Tebbe, C. Kuttner, V. Bieber, V.V. Tsukruk, M. Chanana, T.A. F. König, A. Fery, Strongly Coupled Plasmonic Modes on Macroscopic Areas via Template-Assisted Colloidal Self-Assembly, Nano Lett. 14 (12) (2014) 6863–6871.
[44] L. Tian, E. Chen, N. Gandra, A. Abbas, S. Singamaneni, Gold Nanorods as Plasmonic Nanotransducers: Distance-Dependent Refractive Index Sensitivity, Langmuir 28 (50) (2012) 17435–17442.
[45] B. Sha, W. Gao, S. Wang, F. Xu, T. Lu, Cytotoxicity of titanium dioxide nanoparticles differs in four liver cells from human and rat, Compos. B Eng. 42 (8) (2011) 2136–2144.
[46] X. Han, R. Gelein, N. Corson, P. Wade-Mercer, J. Jiang, P. Biswas, J.N. Finkelstein, A. Elder, G. Oberdörster, Validation of an LDH assay for assessing nanoparticle toxicity, Toxicology 287 (1–3) (2011) 99–104.
[47] W. Zhang, Y. Ji, X. Wu, H. Xu, Trafficking of Gold Nanorods in Breast Cancer Cells: Uptake, Lysosome Maturation, and Elimination, ACS Appl. Mater. Interfaces 5 (19) (2013) 9856–9865.
[48] S. Duclos, R. Corsini, M. Desjardins, Remodeling of endosomes during lysosome biogenesis involves 'kiss and run' fusion events regulated by rab5, J. Cell Sci. 116 (5) (2003) 907–918.
[49] K. Bolaños, M. Sánchez-Navarro, A. Tapia-Arellano, E. Giralt, M.J. Kogan, E. Araya, Oligoarginine Peptide Conjugated to BSA Improves Cell Penetration of Gold Nanorods and Nanoprisms for Biomedical Applications, Pharmaceutics 13 (8) (2021) 1204.
[50] M.T. Larsen, O.A. Mandrup, K.K. Schelde, Y. Luo, K.D. Sørensen, F. Dagnæs-Hansen, J. Cameron, M. Stougaard, T. Steiniche, K.A. Howard, FcRn overexpression in human cancer drives albumin recycling and cell growth; a mechanistic basis for exploitation in targeted albumin-drug designs, J. Control. Release 322 (2020) 53–63.
[51] A.M. Merlot, D.S. Kalinowski, D.R. Richardson, Unraveling the mysteries of serum albumin—more than just a serum protein, Front. Physiol. 5 (2014).
[52] L. Kou, J. Sun, Y. Zhai, Z. He, The endocytosis and intracellular fate of nanomedicines: Implication for rational design, Asian J. Pharm. Sci. 8 (1) (2013) 1–10.
[53] J.E. Deanfield, J.P. Halcox, T.J. Rabelink, Endothelial Function and Dysfunction, Circulation 115 (10) (2007) 1285–1295.
[54] X. Meng, A. Zhou, Y. Huang, Y. Zhang, Y. Xu, K. Shao, X. Ning, N-Cadherin Nanoantagonist Driven Mesenchymal-to-Epithelial Transition in Fibroblasts for Improving Reprogramming Efficiency, Nano Lett. 21 (13) (2021) 5540–5546.
[55] M.G. Lampugnani, Endothelial adherens junctions and the actin cytoskeleton: an 'infinity net'? J. Biol. 9 (3) (2010) 16.
[56] J. Wu, Z. Zhu, W. Liu, Y. Zhang, Y. Kang, J. Liu, C. Hu, R. Wang, M. Zhang, L. Chen, L. Shao, How Nanoparticles Open the Paracellular Route of Biological Barriers: Mechanisms, Applications, and Prospects, ACS Nano 16 (10) (2022) 15627–15652.
[57] A.C. Dumitru, M.A. Poncin, L. Conrard, Y.F. Dufrêne, D. Tyteca, D. Alsteens, Nanoscale membrane architecture of healthy and pathological red blood cells, Nanoscale Horiz. 3 (3) (2018) 293–304.
[58] R. Garcia, Nanomechanical mapping of soft materials with the atomic force microscope: methods, theory and applications, Chem. Soc. Rev. 49 (16) (2020) 5850–5884.
[59] D. Alsteens, R. Newton, R. Schubert, D. Martinez-Martin, M. Delguste, B. Roska, D. J. Müller, Nanomechanical mapping of first binding steps of a virus to animal cells, Nat. Nanotechnol. 12 (2) (2017) 177–183.
[60] A. Calzado-Martín, M. Encinar, J. Tamayo, M. Calleja, A. San Paulo, Effect of Actin Organization on the Stiffness of Living Breast Cancer Cells Revealed by Peak-Force Modulation Atomic Force Microscopy, ACS Nano 10 (3) (2016) 3365–3374.
[61] J. Liu, S. Smith, C. Wang, Reversing the Epithelial-Mesenchymal Transition in Metastatic Cancer Cells Using CD146-Targeted Black Phosphorus Nanosheets and a Mild Photothermal Treatment, ACS Nano 16 (2) (2022) 3208–3220.
[62] J. Liu, L. Kang, S. Smith, C. Wang, Transmembrane MUC18 Targeted Polydopamine Nanoparticles and a Mild Photothermal Effect Synergistically Disrupt Actin Cytoskeleton and Migration of Cancer Cells, Nano Lett. 21 (22) (2021) 9609–9618.
[63] J. Oldenburg, J. de Rooij, Mechanical control of the endothelial barrier, Cell Tissue Res. 355 (3) (2014) 545–555.
[64] J.D. van Buul, I. Timmerman, Small Rho GTPase-mediated actin dynamics at endothelial adherens junctions, Small GTPases 7 (1) (2016) 21–31.
[65] T. Murata, M.I. Lin, R.V. Stan, P.M. Bauer, J. Yu, W.C. Sessa, Genetic Evidence Supporting Caveolae Microdomain Regulation of Calcium Entry in Endothelial Cells *, J. Biol. Chem. 282 (22) (2007) 16631–16643.
[66] G. Sowa, Caveolae, Caveolins, Cavins, and Endothelial Cell Function: New Insights, Front. Physiol. 2 (2012).
[67] Y. Liu, E. Yoo, G.J. Mahler, A.L. Doiron, Endothelial barrier dysfunction induced by nanoparticle exposure through actin remodeling via caveolae/raft-regulated calcium signalling, NanoImpact 11 (2018) 82–91.
[68] Z. Wang, C. Tiruppathi, R.D. Minshall, A.B. Malik, Size and Dynamics of Caveolae Studied Using Nanoparticles in Living Endothelial Cells, ACS Nano 3 (12) (2009) 4110–4116.
[69] J.E. Schnitzer, gp60 is an albumin-binding glycoprotein expressed by continuous endothelium involved in albumin transcytosis, Am. J. Phys. Anthropol. 262 (1 Pt 2) (1992) H246–H254.
[70] A. Minard, C.C. Bauer, D.J. Wright, H.N. Rubaiy, K. Muraki, D.J. Beech, R.S. Bon, Remarkable Progress with Small-Molecule Modulation of TRPC1/4/5 Channels: Implications for Understanding the Channels in Health and Disease, Cells 7 (6) (2018) 52.
[71] R.R. Rigor, Q. Shen, C.D. Pivetti, M.H. Wu, S.Y. Yuan, Myosin light chain kinase signaling in endothelial barrier dysfunction, Med. Res. Rev. 33 (5) (2013) 911–933.

[72] Q. Shen, R.R. Rigor, C.D. Pivetti, M.H. Wu, S.Y. Yuan, Myosin light chain kinase in microvascular endothelial barrier function, Cardiovasc. Res. 87 (2) (2010) 272–280.
[73] D. Mateo, P. Morales, A. Ávalos, A.I. Haza, Oxidative stress contributes to gold nanoparticle-induced cytotoxicity in human tumor cells, Toxicol. Mech. Methods 24 (3) (2014) 161–172.
[74] P. Schlinkert, E. Casals, M. Boyles, U. Tischler, E. Hornig, N. Tran, J. Zhao, M. Himly, M. Riediker, G.J. Oostingh, V. Puntes, A. Duschl, The oxidative potential of differently charged silver and gold nanoparticles on three human lung epithelial cell types, J. Nanobiotechnol. 13 (2015), 1–1.
[75] M.I. Setyawati, C.Y. Tay, S.L. Chia, S.L. Goh, W. Fang, M.J. Neo, H.C. Chong, S. M. Tan, S.C.J. Loo, K.W. Ng, J.P. Xie, C.N. Ong, N.S. Tan, D.T. Leong, Titanium dioxide nanomaterials cause endothelial cell leakiness by disrupting the homophilic interaction of VE–cadherin, Nat. Commun. 4 (1) (2013) 1673.
[76] M.I. Setyawati, C.Y. Tay, B.H. Bay, D.T. Leong, Gold Nanoparticles Induced Endothelial Leakiness Depends on Particle Size and Endothelial Cell Origin, ACS Nano 11 (5) (2017) 5020–5030.
[77] N. Ni, W. Wang, Y. Sun, X. Sun, D.T. Leong, Inducible endothelial leakiness in nanotherapeutic applications, Biomaterials 287 (2022), 121640.
[78] D. Kota, L. Kang, A. Rickel, J. Liu, S. Smith, Z. Hong, C. Wang, Low doses of zeolitic imidazolate framework-8 nanoparticles alter the actin organization and contractility of vascular smooth muscle cells, J. Hazard. Mater. 414 (2021), 125514.